Master Thesis

2D Turbulence spreading

Author:
Víctor Ballester

Supervisors:
Alexandros Alexakis*
Emmanuel Dormy†

Abstract

This thesis investigates the propagation of locally injected turbulence within a doubly periodic 2D domain. Numerical simulations of the Navier-Stokes equations are conducted with localized zero-mean forcing applied. Additionally, a point vortex model is employed to compare vortex evolution between the two approaches. The results demonstrate that the energy carried by vortices spreads across the domain, as opposed to previous works in 3D domains, and reaches domain boundaries regardless of the size of the perturbation region if the Reynolds number is sufficiently high. A power law for the enstrophy distribution as a function of distance from the forcing region is identified, which is also consistent with the results found in the point vortex model.

M2 Mathématiques Appliquées et Théoriques
Université Paris Dauphine - PSL
Laboratoire de Physique de l'École Normale Supérieure

June 30, 2024

*Professor in the Department of Physics at École Normale Supérieure. Webpage: https://www.phys.ens.fr/~alexakis/ (accessed on June 26, 2024)

†Professor in the Department of Mathematics at École Normale Supérieure. Webpage: https://www.math.ens.fr/~dormy/ (accessed on June 26, 2024)

Contents

1 Introduction

Turbulence in fluids is an ubiquitous phenomenon in our daily lives, manifesting in everything from the flow of water in a kitchen sink to the swirling smoke of a cigarette. These examples naturally occur in a three-dimensional (3D) space, as it is the intrinsic dimension of our world. However, this thesis focuses on the study of certain aspects of two-dimensional (2D) turbulence, which might initially seem less realistic. Despite this, 2D turbulence holds significant importance in the field of fluid dynamics. For instance, as explained in Boffetta and Ecke 2012, many large-scale atmospheric and oceanic phenomena exhibit properties closely related to those observed in 2D turbulence, making such phenomena well-approximated at first order by simplified 2D models.

Theoretically, 2D turbulence behaves quite differently from its 3D counterpart, contrary to natural intuition. While in 3D turbulence, energy cascades from large scales to small scales, in 2D turbulence, energy transfers from small scales to large scales. This fundamental difference is directly related to the primary motivation of this work: understanding the flows in the atmosphere. Although the atmosphere is a 3D domain, it is relatively thin in height, allowing for the observation of phenomena typical of 2D turbulence.

This thesis investigates the behavior of 2D turbulence under the influence of a localized inhomogeneous forcing continuously applied to the system. This forcing is responsible for the continuous generation of vortices in the domain. Several questions arise initially: Will the vortices reach the domain boundaries, or will they dissipate as they spread? How does the energy distribution evolve with distance from the forcing region? These questions are thoroughly addressed in this study. Similar questions were explored in Alexakis 2023. In that study the author considered a long periodic 3D box and found that energy does not reach the domain boundaries if the boundaries are sufficiently large, regardless of the Reynolds number. This work tries to extend that study to the 2D case.

In the present study, a doubly periodic 2D box is analyzed with a localized zero-mean forcing applied to the system. The zero-mean nature of the forcing ensures that no net momentum is injected into the system. Additionally, a point vortex model is examined to compare its results with those obtained from the 2D Navier-Stokes equations.

The structure of this thesis is organized as follows: Section 2 details the theoretical framework of our problem and defines all the relevant quantities. Section 3 describes the numerical setup and presents the results obtained during the study. Finally, Section 4 provides conclusions and discusses the implications of our simulations.

2 Theoretical background

The primary focus of this work is the integration of the incompressible Navier-Stokes equations with a random forcing term:

$$\partial_t \boldsymbol{u} + (\boldsymbol{u}\cdot\boldsymbol{\nabla})\boldsymbol{u} = -\boldsymbol{\nabla} p + \nu\Delta\boldsymbol{u} + \boldsymbol{f} \tag{2.1}$$

$$\boldsymbol{\nabla}\cdot\boldsymbol{u} = 0 \tag{2.2}$$

where $\boldsymbol{u}$ is the velocity field, p is the pressure, ν is the kinematic viscosity, and $\boldsymbol{f}$ is a random forcing term satisfying $\boldsymbol{\nabla}\cdot\boldsymbol{f} = 0$. The second equation is called *incompressibility condition* and translates the fact that the fluid cannot be compressed. The forcing term is chosen to be random and delta-correlated in time with Gaussian distribution of amplitudes, for the vorticity formulation, which is detailed below. Throughout the project the density of the fluid is assumed to be constant and equal to 1.

2.1. Stream function formulation

In Batchelor 2000, a new variable is introduced in order to simplify the integration of the 2D incompressible Navier-Stokes equations. This quantity, called *stream function* and denoted by ψ, is defined as the flow rate across a given line. More accurately, if $\mathcal{C}$ is a curve joining two points O (fixed) and $P = (x, y)$, the stream function as a function of the coordinates of the point P is then

$$\psi(x,y) - \psi_0 = \int_{\mathcal{C}} \boldsymbol{u}^\perp \cdot \mathrm{d}\boldsymbol{s} = \int_O^P -v\,\mathrm{d}x + u\,\mathrm{d}y \tag{2.3}$$

where $\boldsymbol{u} = (u, v)$ is the velocity field, $\mathrm{d}\boldsymbol{s} = (\mathrm{d}x\,, \mathrm{d}y)$ is the tangent vector to the curve, and ψ_0 is a reference value. In differential form, it can be written as

$$\mathrm{d}\psi = -v\,\mathrm{d}x + u\,\mathrm{d}y = \frac{\partial\psi}{\partial x}\,\mathrm{d}x + \frac{\partial\psi}{\partial y}\,\mathrm{d}y \tag{2.4}$$

where the last equality follows from the exact differential property. Thus, one obtains the following useful relations:

$$u = \frac{\partial\psi}{\partial y} \quad \text{and} \quad v = -\frac{\partial\psi}{\partial x} \tag{2.5}$$

Note the arbitrary choice of sign of $\boldsymbol{u}^\perp$ in the definition of the stream function. In the present work, the choice is made to be $\boldsymbol{u}^\perp = (-v, u)$, in order to keep the same sign convention as in similar works (Boffetta and Ecke 2012; Alexakis and Biferale 2018). The formulation with the alternative stream function $\psi' := -\psi$ is sometimes used in other fields of fluid dynamics, mostly in meteorology and oceanography.

Note that using this definition, the incompressible condition $\boldsymbol{\nabla}\cdot\boldsymbol{u} = 0$ is automatically satisfied. Finally, introducing the scalar vorticity $\omega := \boldsymbol{\nabla}\times\boldsymbol{u} = \frac{\partial v}{\partial x} - \frac{\partial u}{\partial y} = -\Delta\psi$, one can rewrite the Navier-Stokes equations in terms of the this latter variable:

$$\partial_t\omega + (\boldsymbol{u}\cdot\boldsymbol{\nabla})\omega = \nu\Delta\omega + f_\omega \tag{2.6}$$

$$\boldsymbol{\nabla}\cdot\boldsymbol{\omega} = 0 \tag{2.7}$$

where the rotational has been taken to both sides of Eqs. (2.1) and (2.2) and basic vector identities have been used. The main objects of interest in the vorticity formulation are the *vortices* (see Fig. 2), which according to Saffman 1993 are the local regions on the plane with non vanishing vorticity and surrounded with an irrotational flow.

Now, using the relation between the stream function and the vorticity one obtains:

$$\partial_t\psi + \Delta^{-1}(\boldsymbol{u}\cdot\boldsymbol{\nabla})\Delta\psi = \nu\Delta\psi + f_\psi \tag{2.8}$$

The reader may quickly observe that this equation appears to be more complicated than the first one. However, when transforming the equation to Fourier space, it becomes much more simpler (see Eq. (2.13)), with the advantage of having a scalar function as the main unknown variable (as opposed to the velocity formulation) and removing the incompressible condition (as opposed to the vorticity formulation), which is implicit in the definition of the stream function.

The forcing term is assumed to be random, in particular it is taken of the form:

$$f_\omega(x,y) = f_0 \sum_{i=1}^{10} A_i \exp\left(-\frac{k_\ell^2}{2}\left[(x-x_{i,1})^2 + (y-y_{i,1})^2\right]\right) - A_i \exp\left(-\frac{k_\ell^2}{2}\left[(x-x_{i,2})^2 + (y-y_{i,2})^2\right]\right) \tag{2.9}$$

The quantities A_i follow a uniform distribution between 0 and 1; f_0 represents the amplitude factor of the forcing; k_ℓ quantifies the size of the vortices (thought in Fourier space) so that the vortices injected have size $\sim 1/k_\ell$, and the coordinates $x_{i,j}$, $y_{i,j}$, for $j = 1, 2$ are random variables that position the vortices inside a small disk of radius k_r centered at the origin in a way such that the density of vortices is (almost) constant in the disk. To be more clear, if one expresses the coordinates of the vortices in polar coordinates as $x = r\cos\theta$ and $y = r\sin\theta$, the angular variable is uniformly distributed between 0 and 2π and the radial variable follows a distribution $\sqrt{\mathcal{U}(0, \pi/k_r)}$ where $\mathcal{U}(a, b)$ is the uniform distribution between a and b. Indeed, one can easily check that the probability of finding a vortex inside a thin annulus of with Δr within the perturbation region does not depend on the radius of the annulus r:

$$\mathbb{P}\left(r - \Delta r < \sqrt{\mathcal{U}(0,\pi/k_r)} \le r\right) = \int_{(r-\Delta r)^2}^{r^2} \frac{1}{\pi/k_r}\,\mathrm{d}s \simeq Cr\Delta r + \mathcal{O}(\Delta r^2) \tag{2.10}$$

Thus, since the area of the annulus $\{(x,y) \in \mathbb{R}^2 : r - \Delta r < \sqrt{x^2+y^2} \le r\}$ is proportional to $r\Delta r$ at first order, the density of vortices is constant, up to a small error of order Δr, throughout the perturbation region.

With this forcing the aim is to introduce pairs of vortices with opposite vorticity in a inhomogeneous way which a priori may seem to introduce a non-zero momentum to the system. To correct that, the first Fourier coefficient is set to zero once transformed the forcing term to Fourier space. This implies that the actual force differs up to a constant factor from the one given above, which from now on it will be assumed that this factor is implicit in f_ω, that is, $\mathbb{E}(f_\omega) = 0$.

The amplitude of the forcing is controlled by the parameter f_0, which is chosen such that injection rate of energy remains constant and equal to 1. Because of that it has an implicit dependence on time, as explained below.

Forward-transforming f_ω to Fourier space, from the relation $\omega = -\Delta\psi$, one can easily get $\widehat{f_\psi}$ by dividing by k^2 each mode of $\widehat{f_\omega}$, being k the norm value of the wave vector.

2.2. Fourier space

The *Fourier transform* (FT) of a function $f : \mathbb{R}^2 \to \mathbb{R}$ is defined as

$$\widehat{f}(\boldsymbol{\xi}) = \int_{\mathbb{R}^2} f(\boldsymbol{x}) \mathrm{e}^{-\mathrm{i}\boldsymbol{\xi}\cdot\boldsymbol{x}}\,\mathrm{d}\boldsymbol{x} \tag{2.11}$$

for all $\boldsymbol{\xi} \in \mathbb{R}^2$ and its discrete version (DFT) for a square domain with N points in each direction is

$$\widehat{f}(\boldsymbol{k}) = \sum_{\boldsymbol{n}\in\boldsymbol{N}} f_{\boldsymbol{n}} \mathrm{e}^{-\mathrm{i}\boldsymbol{k}\cdot\boldsymbol{n}/N} \tag{2.12}$$

where $\boldsymbol{N} = \{0, 1, \ldots, N-1\}^2$ is the set of points in the Fourier grid, $f_{\boldsymbol{n}}$ is the value of the function in the physical space at point $\boldsymbol{n}$, and $\boldsymbol{k} = (k_x, k_y)$ is the wave vector.

Taking the Fourier transform on both sides of Eq. (2.8) and using the well-known properties of the Fourier transform, one obtains:

$$\frac{\mathrm{d}}{\mathrm{d}t}\widehat{\psi} - k^{-2}\widehat{(\boldsymbol{u}\cdot\boldsymbol{\nabla})\Delta\psi} = -\nu k^2\widehat{\psi} + \widehat{f_\psi} \tag{2.13}$$

where $k := \|\boldsymbol{k}\|$. Note that the non-linear term in the above equation has not been simplified. This is because in the simulation that term is backward-transformed to the physical space, computed, and then transformed back to the Fourier space, as it is less expensive and simpler than computing the non-linear term in Fourier space.

2.3. *Reynolds number*

The Reynolds number is a dimensionless quantity that characterizes the ratio of inertial forces to viscous forces in a fluid. It is usually defined as $\mathrm{Re} := UL/\nu$, where U is a characteristic velocity of the flow, L is the characteristic length scale associated to it and ν is the kinematic viscosity. In the cases where there is no control on the injection velocity, but instead one can control the rate of energy injection ϵ, this equation is not useful anymore. To derive an alternative equation, the scaling theory of Kolmogorov is used (Frisch 1995). Let $\epsilon_\ell \sim u_\ell^2/\tau_\ell$ be the rate of change of energy at the scale ℓ, where u_ℓ is the typical velocity at that scale and τ_ℓ is the characteristic time at that scale. Using that $\tau_\ell \sim \ell/u_\ell$, one obtains $\epsilon_\ell \sim u_\ell^3/\ell$. Assuming that the energy transferred from the scale ℓ to smaller scales is the same as the energy received by the scale ℓ from larger scales (that is, the flux of energy across scales is constant), one obtains that the value ϵ does not depend on ℓ and moreover $\epsilon \sim U^3/L$, i.e. $U \sim (\epsilon L)^{1/3}$. Thus, one obtains a new formula for the Reynolds number:

$$\mathrm{Re} = \frac{\epsilon^{1/3} L^{4/3}}{\nu} \tag{2.14}$$

In the present work, the length scale L is determined by the size of the vortices injected in the disk, which in this case is $L = 1/k_\ell$. The injection rate of energy is determined by the forcing term, as follows. The amplitude f_0 is time dependent and is chosen in such a way that f_0^2 is the rate at which energy is injected per unit of area in the domain. More precisely, the amplitude of the forcing is taken as $f_0/\sqrt{\Delta t/2}$, where Δt is the time step of the simulation, a priori varying with time.

To check that indeed this is the case, let $\boldsymbol{f} = \frac{f_0}{\sqrt{\Delta t/2}}(f_u, f_v)$ be the forcing term for the velocity equation in the physical space. Recall that since $\mathbb{E}(f_\omega) = 0$ and $f_\omega = \boldsymbol{\nabla}\times \boldsymbol{f}$, using the inversion formula for the curl (see Eq. (2.26)) and Fubini's theorem one obtains that $\mathbb{E}(f_u) = \mathbb{E}(f_v) = 0$. Thus, at time $t = T$ and time step Δt one has, taking into account only the forcing term:

$$u(\boldsymbol{x}, T + \Delta t) = u(\boldsymbol{x}, T) + \Delta t \, \frac{f_0}{\sqrt{\Delta t/2}} \, f_u(\boldsymbol{x}) + \cdots \tag{2.15}$$

Squaring both sides of the equation one obtains:

$$u(\boldsymbol{x}, T + \Delta t)^2 = u(\boldsymbol{x}, T)^2 + 2\sqrt{2\Delta t}\, f_0 f_u(\boldsymbol{x}) u(\boldsymbol{x}, T) + 2\Delta t\, f_0^2 f_u(\boldsymbol{x})^2 + \mathcal{O}(\Delta t^{3/2}) \tag{2.16}$$

Taking expectation on both sides one concludes that:

$$\frac{u(\boldsymbol{x}, T + \Delta t)^2 - u(\boldsymbol{x}, T)^2}{\Delta t} = 2 f_0^2 \, \mathbb{E}(f_u(\boldsymbol{x})^2) \tag{2.17}$$

where the second term on Eq. (2.16) vanishes because of the zero-mean property of the forcing term. Doing a similar computation for the v component, summing both equations and taking the limit $\Delta t \to 0$, one obtains the rate of energy injected in the domain.

$$\frac{\partial E}{\partial t} = \frac{1}{2}\frac{\partial}{\partial t}(u^2 + v^2) = f_0^2 \, \mathbb{E}(f_u^2 + f_v^2) \tag{2.18}$$

The implicit assumption that $\rho = 1$ in the equation ensures that it precisely represents the rate of energy injected per unit of area in the domain. In the simulations at each step the amplitude of the forcing term is adjusted so that its variance is equal to 1, making the rate of energy injection become f_0^2. Since the interest is, not on the injection rate of energy per unit of area, but on the injection rate of energy per unit of area in the forcing region, the following formula for ϵ is used:

$$\epsilon = f_0^2 \, \frac{4\pi^2}{\pi(\pi/k_r)^2} \tag{2.19}$$

because the area of the whole domain considered $[-\pi, \pi]\times[-\pi, \pi]$ is $4\pi^2$ and the area of the forcing region is $\pi(\pi/k_r)^2$. Consequently the Reynolds number becomes:

$$\mathrm{Re} = \frac{\left(f_0^2 \, \frac{4k_r^2}{\pi}\right)^{1/3} k_\ell^{-4/3}}{\nu} \tag{2.20}$$

2.4. Point vortex model

The study has been complemented by another simulation, far from the Navier-Stokes equations, but aiming to obtain qualitatively and quantitatively similar results. This simulation is based on the point vortex model, which is a simplified version of the dynamics of a set of vortices.

More precisely, in the point vortex model that follows, the viscous term is neglected. Thus, this problem aims to mimic in some way the dynamics of the Navier-Stokes equations as $\nu \to 0$ (or equivalently $\mathrm{Re} \to \infty$, see Eq. (2.20)). Moreover, vortices are considered as point-like objects, that is to say, being the vorticity singular at the position of the vortices. Because of that, the vortices are characterized by their circulation

$$\Gamma = \lim_{\mathrm{diam}(\mathcal{C})\to 0} \int_{\mathcal{C}} \boldsymbol{u} \cdot \mathrm{d}\boldsymbol{s} \tag{2.21}$$

where $\mathcal{C}$ is a curve surrounding the vortex. In those conditions and in absence of external forces, the vorticity field ω is only advected and its evolution in time is described by the following transport equation:

$$\partial_t \omega + (\boldsymbol{u} \cdot \boldsymbol{\nabla})\omega = 0 \tag{2.22}$$

together with the incompressible condition $\boldsymbol{\nabla} \cdot \boldsymbol{u} = 0$ (Ceci and Seis 2022). Here $\boldsymbol{u}$ is the velocity field generated by the vortices. An interesting interpretation of the vortices involves the Dirac's delta distribution. Specifically, the vorticity field generated by a point vortex located at $\boldsymbol{y}$ can be represented as a distribution of the form:

$$\omega(\boldsymbol{x}, t) = \Gamma \delta(\boldsymbol{x} - \boldsymbol{y}) \tag{2.23}$$

where Γ is the circulation of the vortex (Saffman 1993). The dynamics of N point vortices in the $\mathbb{R}^2$ plane are described in the following theorem:

Theorem 1. Consider N vortices at positions $\boldsymbol{z}_1, \ldots, \boldsymbol{z}_N \in \mathbb{R}^2$ with circulations $\Gamma_1, \ldots, \Gamma_N$. Then, their evolution in time is described by the following system of ordinary differential equations (Aref 2007):

$$\dot{x}_i = -\sum_{j \neq i} \frac{\Gamma_j}{2\pi} \frac{y_i - y_j}{(x_i - x_j)^2 + (y_i - y_j)^2} \tag{2.24}$$

$$\dot{y}_i = \sum_{j \neq i} \frac{\Gamma_j}{2\pi} \frac{x_i - x_j}{(x_i - x_j)^2 + (y_i - y_j)^2} \tag{2.25}$$

for $i = 1, \ldots, N$, where $\boldsymbol{z}_i = (x_i, y_i)$.

Proof. Since there is no viscosity in the equations, each vortex is advected with the velocity field generated by all the other vortices. Now, given $\boldsymbol{f} \in \mathcal{C}^1(\mathbb{R}^2, \mathbb{R}^2)$ such that $\boldsymbol{\nabla} \cdot \boldsymbol{f} = 0$ and $g := \boldsymbol{\nabla} \times f$, by Biot-Savart law one can invert the curl operator using the Biot-Savart kernel (see Griffiths 2023):

$$\boldsymbol{f}(\boldsymbol{x}) = (\boldsymbol{K} * g)(\boldsymbol{x}) = \int_{\mathbb{R}^2} \boldsymbol{K}(\boldsymbol{x} - \boldsymbol{y}) g(\boldsymbol{y}) \, \mathrm{d}\boldsymbol{y} \tag{2.26}$$

where $\boldsymbol{K}(\boldsymbol{x}) = \dfrac{1}{2\pi} \dfrac{(-x_2, x_1)}{\|\boldsymbol{x}\|^2}$ is the Biot-Savart kernel and $\boldsymbol{x} = (x_1, x_2)$. In our case, $\boldsymbol{g}$ is the vorticity field which is a sum of δ's. Thus, taking into consideration Eq. (2.23), the velocity field generated by a vortex at $\boldsymbol{z}_j$ with circulation Γ_j is:

$$\boldsymbol{u}_j(\boldsymbol{x}) = \boldsymbol{K}(\boldsymbol{x} - \boldsymbol{z}_j)\Gamma_j \tag{2.27}$$

The proof concludes using the superposition principle. □

The reader should not confuse the notation N here, which denotes the number of vortices, with the notation N in the Navier-Stokes equations, which denotes the number of points in the physical space.

Another aspect worth-mentioning is the numerical addition of a softening parameter ε to Eqs. (2.24) and (2.25) in order to prevent the positions of the vortices from blowing up when two vortices get too

close to each other. The equations then take the following form:

$$\dot{x}_i = -\sum_{j\neq i} \frac{\Gamma_j}{2\pi} \frac{y_i - y_j}{(x_i - x_j)^2 + (y_i - y_j)^2 + \varepsilon^2} \tag{2.28}$$

$$\dot{y}_i = \sum_{j\neq i} \frac{\Gamma_j}{2\pi} \frac{x_i - x_j}{(x_i - x_j)^2 + (y_i - y_j)^2 + \varepsilon^2} \tag{2.29}$$

This adjustment avoids the singularities of the system. These singularities occur when two vortices get too close to each other, which in Section 3.2 is shown to be the common behavior of the system. The softening parameter is chosen to be $\varepsilon = 0.001$, being this value small enough not to affect the dynamics of the system but large enough to prevent a numerical blow-up.

In order to narrow the gap between the point vortex model and the Navier-Stokes equations while keeping the simplicity of the former, a set of vortices is added regularly in time to simulate the action of a forcing term in the equations. The point vortices are added in a similar way as in the Navier-Stokes, but this time making the addition completely symmetric to cancel out any non-zero momentum that could be introduced in the system.

2.5. Monitored quantities

In order to keep track of the evolution of the system, several variables are monitored during the simulation.

For the Navier-Stokes equations, the main quantity of interest is the total energy and vorticity in the system. Since the work environment is the Fourier space (see Section 3.1), the energy is computed as

$$E = \sum_{\boldsymbol{k}\in\boldsymbol{K}} \|\widehat{\boldsymbol{u}}(\boldsymbol{k})\|^2 = \sum_{\boldsymbol{k}\in\boldsymbol{K}} k^2 |\widehat{\psi}(\boldsymbol{k})|^2 \tag{2.30}$$

which by the Parseval identity is equivalent to the total energy in the physical space. Here $\boldsymbol{K} = \{0, 1, \ldots, K-1\}^2$ is the set of points in the Fourier grid, and $K = N/3$ is the maximum wave number chosen in order to control the aliasing effects. Another important quantity worth-considering is *enstrophy*, which is analogous to energy but uses vorticity instead of velocity as the primary variable. It is defined as

$$\Omega = \sum_{\boldsymbol{k}\in\boldsymbol{K}} |\widehat{\omega}(\boldsymbol{k})|^2 = \sum_{\boldsymbol{k}\in\boldsymbol{K}} k^4 |\widehat{\psi}(\boldsymbol{k})|^2 \tag{2.31}$$

where the second equality follows from the relation $\omega = -\Delta\psi$.

As the title suggests, the main purpose of this work is to study how turbulence is spread across the domain. Thus, quantities relating the energy and enstrophy contained in annuli as a function of the radius of the annuli are also taken into account. These variables are respectively denoted by E_r and Ω_r, and they are given by the following expressions:

$$E_r = \sum_{r-\Delta r<\|\boldsymbol{x}\|\leq r} \|\boldsymbol{u}(\boldsymbol{x})\|^2 \tag{2.32}$$

$$\Omega_r = \sum_{r-\Delta r<\|\boldsymbol{x}\|\leq r} |\omega(\boldsymbol{x})|^2 \tag{2.33}$$

where $r \in (\Delta r, \pi)$. The quantities E_r and Ω_r are then plotted as a function of r in order to study the energy and enstrophy distribution across the domain (see Section 3.2).

Related to these variables are the mean energy radius and mean enstrophy radius, which denote a weighted average of the radius, intuitively representing where the majority of energy and enstrophy reside. They are defined as:

$$\mathcal{R}_E^2 = \frac{\sum_{\Delta r<r\leq\pi} r^2 E_r}{\sum_{\Delta r<r\leq\pi} E_r} \quad \text{and} \quad \mathcal{R}_\Omega^2 = \frac{\sum_{\Delta r<r\leq\pi} r^2 \Omega_r}{\sum_{\Delta r<r\leq\pi} \Omega_r} \tag{2.34}$$

Note that since the domain is square, the sums $\sum_{\Delta r<r\leq\pi} E_r$ and $\sum_{\Delta r<r\leq\pi} \Omega_r$ are slightly less than the total energy E and enstrophy Ω respectively, since they account for the contributions from the different annuli in the domain until their radii reach the radius of the incircle of the square.

Regarding the point vortex model, the system is integrable and the following function H

$$H = \sum_{i=1}^{N} H_i, \qquad H_i = -\frac{1}{4\pi} \sum_{j \neq i} \Gamma_j \log \|\boldsymbol{z}_i - \boldsymbol{z}_j\|^2 \tag{2.35}$$

is a first integral of the system. Moreover the system is Hamiltonian, that is, it can written as:

$$\dot{x}_i = \frac{\partial H}{\partial y_i} \tag{2.36}$$

$$\dot{y}_i = -\frac{\partial H}{\partial x_i} \tag{2.37}$$

At first sight, the reader may notice that the function H is singular when two vortices get too close to each other. Although one could try to create an auxiliary function $f(H)$ that is regular in the whole domain and has a shape according the physical intuition while keeping the properties of a first integral, an alternative approach was chosen in this work to mimic the energy and enstrophy profiles for the Navier-Stokes equation.

The idea explored here involves counting the number of point vortices in annuli and comparing the density distribution ρ_r with the corresponding functions E_r and Ω_r. Specifically, the density of vortices ρ_r is defined as the density of vortices in the ring of radius r, that is:

$$\rho_r = \lim_{\Delta r \to 0} \frac{N_r}{2\pi r \Delta r} \tag{2.38}$$

where $N_r = N_r(\Delta r)$ is the number of vortices in the annulus of radius r and width Δr.

Additionally, an equivalent mean radius is defined, which gives an insight on the average location of the vortices within the domain. Its expression is given by:

$$\mathcal{R}_N^2 = \frac{\sum_{\Delta r < r \leq \pi} r^2 N_r}{\sum_{\Delta r < r \leq \pi} N_r} \tag{2.39}$$

3 Simulation

3.1. Numerical setup

The 2D incompressible Navier-Stokes equations are forced in a periodic domain of size $2\pi \times 2\pi$ with a forcing term that is located in a disk of radius π/k_r centered at the origin. The range of values for the parameter k_r is taken to be $\{8, 16, 32, 64\}$ and in all the cases the size of the vortices, which is controlled by k_ℓ, is set to $k_\ell = 4k_r$. The parameter k_r being one of those values in the previous set represents how smaller the perturbation region is (in diameter) compared to the domain size (2π). The other parameter k_ℓ accounts for the size of the vortices, as $1/k_\ell$ gives a typical length scale of the vortices. Fig. 1 shows a graphical representation of the forcing term for two different values of k_r.

The Reynolds number is the other parameter that plays an important role in the whole simulation. This project has simulated fluid flows for Reynolds numbers within the set $\{0.25, 0.5, 1, 2, 4, 8, 16, 32, 64, 128\}$, each of those requiring different resolution as the Reynolds number is increased in order to capture the smallest scales where energy gets dissipated by viscosity.

A pseudo-spectral method is used to solve the Navier-Stokes equations, based on the Fourier basis and then using an improved 2nd-order low-storage Runge-Kutta method to integrate the resulting ordinary differential equation. As explained in Brachet et al. 2008, this method differs from the conventional Runge-Kutta methods by reducing the amount of storage needed for each iteration at the expense of roughly doubling the time needed for evaluating the temporal derivatives at the same order as the usual Runge-Kutta methods. Specifically, if $\widehat{\boldsymbol{\psi}}_n$ is the vector containing all the coordinates at the n-th step of the integration, the scheme follows the subsequent steps:

1. Copy $\widehat{\boldsymbol{\psi}}_n$ into $\widehat{\boldsymbol{\psi}}_*$.
2. For $i = s, \ldots, 1$, s being the number of stages of the Runge-Kutta method, update $\widehat{\boldsymbol{\psi}}_*$ as follows:

$$\widehat{\boldsymbol{\psi}}_* \leftarrow \widehat{\boldsymbol{\psi}}_n + \Delta t \frac{\boldsymbol{F}(\widehat{\boldsymbol{\psi}}_*)}{i} \tag{3.1}$$

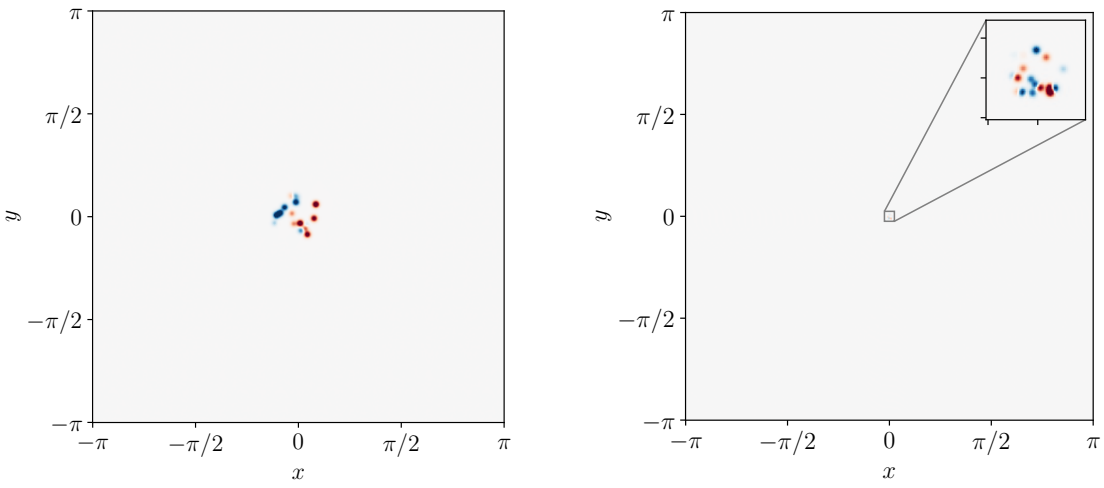

(a) $k_r = 8$ **(b)** $k_r = 64$

Figure 1: Vorticity forcing term for different values of k_r. Red colors and blue colors mean different direction of rotation for each vortex. The reader may notice that indeed in the first plot the diameter of the forcing region is about 8 times smaller than the total size of the domain. In the second plot, this property is less noticeable, but it is still true, this case being 64 times smaller.

where $\boldsymbol{F}$ represents the field that defines the differential equation for $\widehat{\psi}$.

3. Set $\widehat{\boldsymbol{\psi}}_{n+1} := \widehat{\boldsymbol{\psi}}_*$.

In the second step, the evaluation of $\boldsymbol{F}$ is done in an explicit-exact manner. This means that the non-linear term is treated explicitly in time, while the linear terms are solved exactly using their exponential solution. For more information about the scheme, the reader is encouraged to read the article from Brachet et al. 2008 or check the source codes in the link provided below. In this work, $s = 4$ is used for all simulations. While this produces a formal order of accuracy of 2, the errors are generally smaller compared to those of a standard second-order Runge-Kutta method.

The codes are run in two supercomputer centers, IDRIS[1] and MESOPSL[2], using 40 to 80 cores, depending on the simulation. Two different kinds of simulations are performed: (fully) parallel simulations and embarrassingly parallel simulations. In the parallel simulations, the Fourier domain is divided among all the processors, allowing them to work simultaneously on different parts of the problem. In the embarrassingly parallel simulations, each simulation runs independently on a single core. Multiple simulations are executed concurrently, one on each available core, and the results are averaged afterwards to obtain more accurate conclusions. This project uses MPI compilers to do the parallelism. Details about the parallelization of the code will not be delved into, but the main idea will be explained.

They key piece of the parallelization of any pseudo-spectral method is the efficient computation of the multidimensional Fourier transform. As a starting point, one of the dimensions of the physical domain, of size $N \times N$, is split, creating several subdomains of sizes $\tilde{N} \times N$, where $\tilde{N} \simeq N/N_{\text{cores}}$ and N_{cores} is the number of cores used. Each core is responsible for computing $\tilde{N}$ 1D real-to-complex Fourier transforms using the standard Fast Fourier Transform (FFT) algorithm which reduces the operations from $\mathcal{O}(N^2)$, using the naive approach, to $\mathcal{O}(N \log N)$. Since the initial data is real-valued, the complex-valued transformed data is then stored in an array $\tilde{N} \times (N/2 + 1)$, which is enough to store all the necessary information. Next, MPI communication is carried out in order to gather all the data, transpose it, and then split it again to produce slices of size $\bar{N} \times N$, where $\bar{N} \simeq (N/2 + 1)/N_{\text{cores}}$. Each core is, similarly as before, responsible for computing $\bar{N}$ 1D complex-to-complex Fourier transforms. Finally, all the data is gathered again to produce the desired FFT resulting in a memory block of size $(N/2+1) \times N$ consisting of complex-valued numbers. If the reader is interested in the details, the article from Mininni et al. 2011 is highly recommended.

[1]For more information about the resources they provide, check their website: http://www.idris.fr/ (accessed on June 30, 2024).

[2]For more information about the resources they provide, check their website: https://wwwmesopsl-new.obspm.fr/ (accessed on June 30, 2024).

For the parallel code, a variable time step is used throughout the whole simulations in order to take into account the advection stability condition. For the embarrassingly parallel code, a fixed time step is used, for the purpose of better comparing the results between the different runs from the same simulation. The time step is chosen by eye after studying the evolution of the time steps during the variable-time-step fully parallel simulations. Table 1 shows the different simulations performed during the project as well as the resolution in physical space used in each case.

k_r \ Re	0.25	0.5	1	2	4	8	16	32	64	128
8	✓$_{512}$	✓$_{512}$	✓$_{512}$	✓✓$_{512}$	✓✓$_{1024}$	✓✓$_{1024}$	✓✓$_{1024}$	✓✓$_{2048}$	✓$_{2048}$	✓$_{4096}$
16				✓$_{1024}$	✓$_{2048}$	✓✓$_{2048}$	✓✓$_{2048}$	✓✓$_{2048}$	✓$_{4096}$	✓$_{4096}$
32				✓$_{2048}$	✓$_{4096}$	✓✓$_{4096}$	✓✓$_{4096}$	✓✓$_{4096}$	✓$_{8192}$	✓$_{8192}$
64						✓$_{8192}$	✓$_{8192}$	✓$_{8192}$		

Table 1: Simulations carried out during the study varying the Reynolds number and the forcing parameter k_r. In all cases k_ℓ is taken as $k_\ell = 4k_r$. The green checkmark symbols indicate the simulations executed in parallel, splitting the domain between different cores. The blue checkmark symbols indicate the simulations conducted in an embarrassingly parallel manner, where each simulation runs independently across multiple cores simultaneously to generate statistical results. In each cell, the number indicates the resolution in each dimension employed, which have been proved (a posteriori) to be enough to well-resolve the system.

The reader may observe that the resolution increases as both the Reynolds number and the forcing parameter k_r increase. For the former, the resolution is increased to resolve the smaller scales that appear in the system, which play an essential role in dissipating energy through viscosity. Thus, as Re increases, ν decreases, and the predicted Kolmogorov wave number, where dissipation occurs, becomes larger. For the latter, the resolution is increased as the wave numbers of the forcing region rise, thereby shifting the energy injection to higher frequencies. It is worth-noting that the resolution in Fourier space is not the same as the one in physical space. Specifically, as mentioned before, the Fourier resolution is one third of the physical resolution in each dimension. This adjustment is made to avoid common aliasing errors that may arise when computing non-linear terms in Fourier space. Concerning the total time of integration, the simulations were stopped when enough vortices had reached the boundaries of the domain, which was determined by eye.

The system of differential equations modeling the point vortex dynamics (see Eqs. (2.28) and (2.29)) is integrated using a Runge-Kutta (7)8 method with adaptive time-stepping based on the Fehlberg error estimate. Briefly, these adaptative Runge-Kutta methods are based on the idea of using two different approximations of the solution at each step, in this case, one of order 7 and another of order 8. Then, the difference between both approximations is used to estimate the error between one of the approximations and the real solution. If the error is below a certain threshold, the time step is increased, and if it is above it, the time step is decreased. The simulations for the point vortex model are conducted, as opposed to the integration of the Navier-Stokes equations, in a personal computer and in a single core. In this latter simulation there is only one parameter to control, which is the radius of the perturbation region, k_r. As the simulation is less computationally expensive, the range of values for k_r is increased to $\{8, 16, 32, 64, 128, 256\}$ compared to the Navier-Stokes simulations.

All the codes and data used for the simulations as well as animations of the dynamics of both problems are available in the following repository: https://github.com/victorballester7/final-master-thesis (accessed on June 26, 2024). The pseudo-spectral codes on that repository are based on previous works from Pablo Mininni[‡] and Alexandros Alexakis. The repository of Pablo Mininni is available at https://github.com/pmininni/GHOST (accessed on June 25, 2024).

3.2. Results

The results of the simulations are presented in this section. The first part is devoted to the results of the Navier-Stokes simulations, while the second part is dedicated to the results of the point vortex simulations.

[‡]Professor in the Department of Physics at the University of Buenos Aires. Webpage: http://wp.df.uba.ar/mininni/ (accessed on June 25, 2024).

We start showing how the vortices spread across the domain in a visual manner.

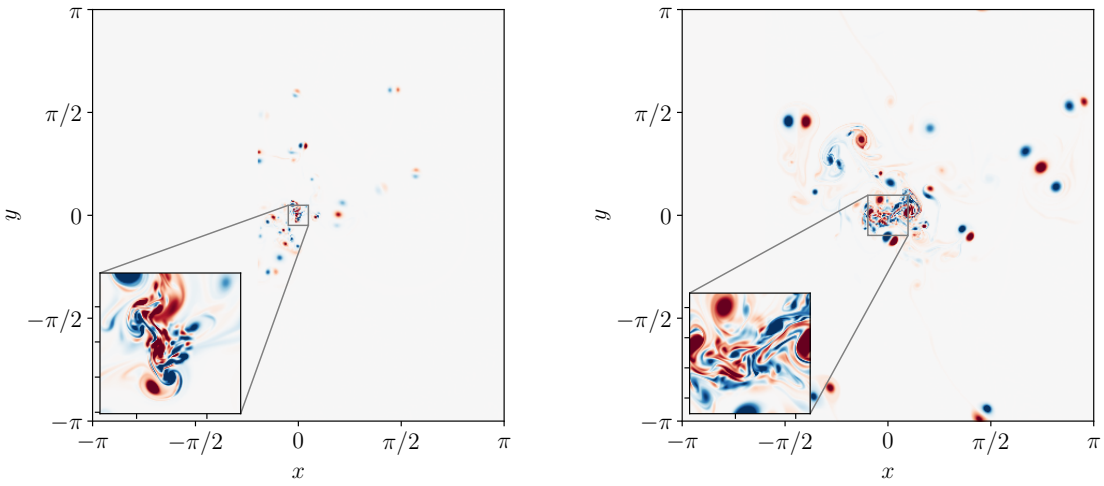

(a) $k_r = 64$, Re $= 32$ **(b)** $k_r = 16$, Re $= 128$

Figure 2: Vorticity plots for different values of k_r and Re. The left-hand side figure is integrated with a resolution of 8192×8192 and the right figure is integrated with a resolution of 4096×4096.

Fig. 2 shows the vorticity plot at two different time slices for the driven Navier-Stokes equation. The most notable feature is that the vortices appear more intense in the plot on the right compared to the plot on the left. This can be attributed to two main reasons. Firstly, the Reynolds number is smaller in the left-hand-side plot, causing dissipation by viscosity to have a more significant impact, leading to a quicker decay of the intensity of the vortices. Secondly, the initial size of the vortices in the plot on the left is four times smaller than in the plot on the right, which restricts their growth in size as time progresses.

With this glimpse into the dynamics of the system, we now proceed to analyze the energy and enstrophy distributions. The following set of plots in Fig. 3 show the energy and enstrophy evolution as a function of the distance to the center of the forcing disk in three different categories: firstly, a Reynolds number and a parameter k_r are picked and the distributions of energy and enstrophy are plotted for different times; secondly, plots varying k_r at fixed time $t = 1.66$ and for Re $= 32$ are shown, and finally, the energy and enstrophy profiles for different Reynolds numbers at fixed time $t = 1.75$ and $k_r = 16$ are displayed. All the data is obtained by averaging the results of 48 simulations, each one with a different random seed, using embarrassingly parallel simulations.

The first feature that the reader may extract from all the plots is that generally the power laws that the quantities appear to follow are more clear and consistent in the vorticity plots, rather than in the energy ones. This, together with the fact that the vorticity plots are more spiky and the energy plots smoother, may be attributed to the fact that vorticity is a quantity more localized than energy, taking only high values where the vortices are located (see Fig. 2). On the other hand, the energy is more widely distributed across the domain because it is proportional to the square of the velocity, unlike vorticity, which depends on the rotation of the fluid. In a sense, this implies that there is more data available for averaging the energy than for the enstrophy, hence the smoother profiles in the energy plots.

On the top two plots of Fig. 3, an increase of energy to outer rings of the domain is observed as time increases, which starts answering one of the initial questions posed in the introduction about whether the energy would remain localized around the perturbation region. In the analogous vorticity plot at larger rings, more variance is observed in the curves for $t = 0.4$ and $t = 0.8$, compared to the curves for $t = 1.3$ and $t = 1.79$. This is attributed to the fact that in some simulations, only a few vortices manage to reach those outer layers of the domain at early times, unlike at later times when most simulations already contain many vortices in those outer layers.

The middle plots show the same evolution of the profiles of energy and enstrophy as a function of the radius of the annuli inside the domain. The most noticeable characteristic on the vorticity plot is that the supposed power law extends to smaller radii as k_r increases. This is expected, as a larger k_r is equivalent to decreasing the size of the forcing region, thereby shifting the observed features associated

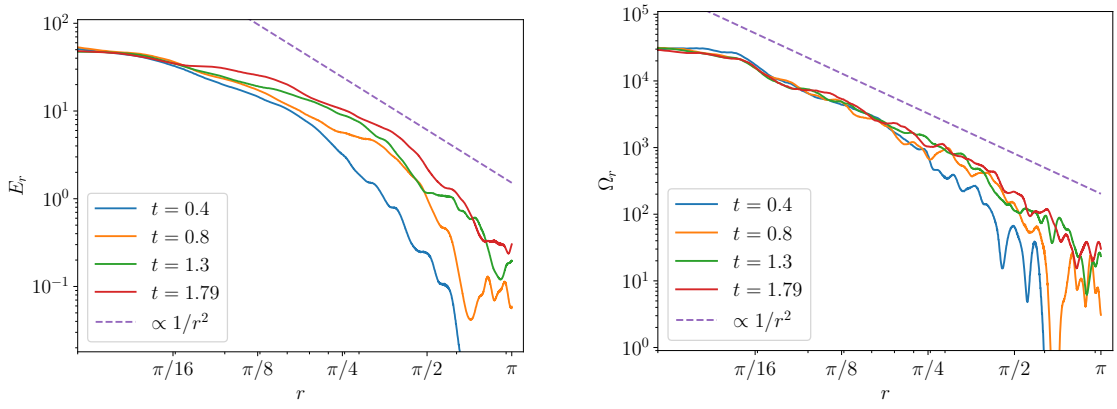

(a) $k_r = 16$, Re $= 16$

(b) $k_r = 16$, Re $= 16$

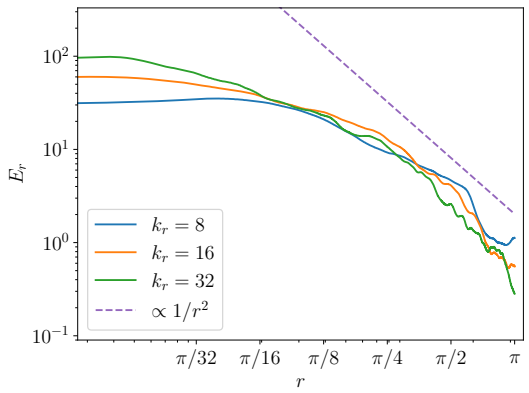

(c) Re $= 32$

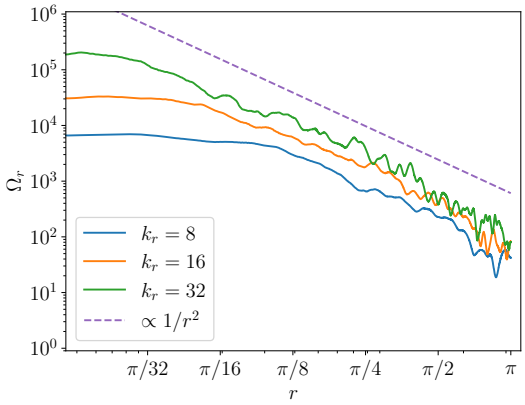

(d) Re $= 32$

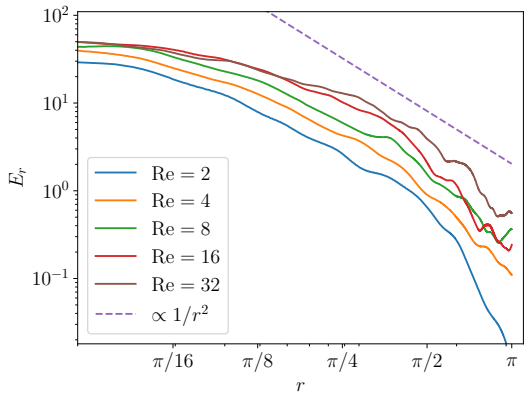

(e) $k_r = 16$

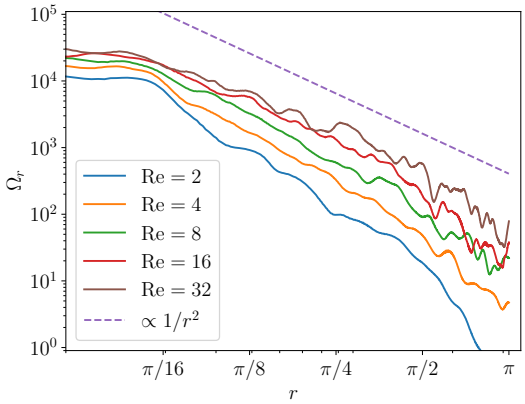

(f) $k_r = 16$

Figure 3: Energy and enstrophy profiles for different values of time, k_r and Re. The left-hand side figures show the respective plots for the energy while in the right-hand side, the enstrophy profiles are displayed. The top plots show the profiles for different slices of time for a fixed $k_r = 16$ and Re $= 16$. The units of time are those determined from the Reynolds number, that is $k_\ell^{-4/3}/\epsilon^{1/3}$, where ϵ is given in Eq. (2.19). The middle plots show the profiles for several radius of the perturbation region at fixed time $t = 1.66$ and fixed Re $= 32$. The bottom plots show the profiles for different Reynolds numbers at fixed time $t = 1.75$ and fixed $k_r = 16$. In all the plots the dashed line represents a function of the form $f(r) = A/r^2$ with A being a constant.

with smaller k_r to different spatial locations, earlier in space. Moreover, before the power law is reached, the vorticity profiles show a roughly constant profile, which indicates the presence of a region where the vortices are equally distributed, i.e. the perturbation region. Indeed, the reader may observe that this roughly constant part of each curve finishes for $k_r = 8$ at $\simeq \pi/8$, for $k_r = 16$ at $\simeq \pi/16$ and for $k_r = 32$ at $\simeq \pi/32$. With the energy profiles, a similar but less pronounced behavior is observed, which aligns

with the previous argument regarding the smoothness of the energy profiles.

Finally, the bottom plots show, at fixed k_r and fixed time, energy and enstrophy profiles for several Reynolds numbers. The remarkable feature here is that an increase in magnitude of both quantities is seen as the Reynolds number increases. This is expected, as viscosity in lower Reynolds numbers plays a more important role in dissipating energy, thereby stabilizing the dynamics of the system. The reader may also observe the constant behavior of the profiles for the range of $r \in [0, \pi/16]$ in the vorticity plots, which is consistent with the previous observations.

Next, the quantities $\mathcal{R}_E$ and $\mathcal{R}_\Omega$ are computed for the Navier-Stokes simulations and their evolution in time is plotted in Fig. 4 for several values of the Reynolds number and fixing the size of the perturbation region to $k_r = 16$.

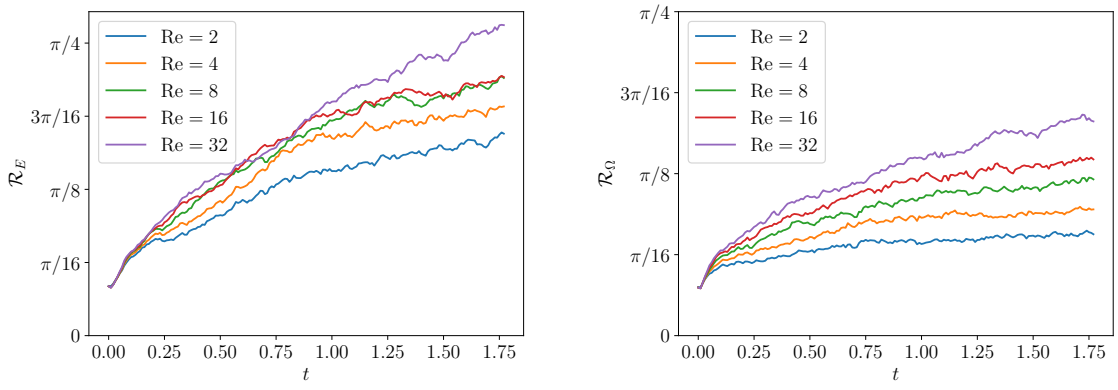

(a) Energy mean radius

(b) Enstrophy mean radius

Figure 4: Mean energy radius and mean enstrophy radius for several runs varying the Reynolds number at fixed $k_r = 16$.

In all cases it is observed an increasing tendency, although the rate changes in time and also in the Reynolds number. Specifically in the enstrophy plot a separation between the different plots can be clearly seen, but the range of $\mathcal{R}_\Omega$ is smaller than the one of $\mathcal{R}_E$, likely due to the localizing nature of the vorticity. Based on this data, it is plausible to conclude that no matter how small the forcing region is, energy spreads throughout the entire domain given enough time, provided that viscosity is sufficiently low to allow vortices to persist without dissipating. It is understood that in order to properly and securely claim this statement, the simulations should have been run for longer times and higher Reynolds numbers.

The second part of this section is reserved to the results of the point vortex simulations. Here vortices are input at a constant rate in the center of the domain and they are removed whenever they reach the boundary of the box. Vortices are defined in terms of their circulation which is assumed to follow a standard normal distribution for all vortices. Fig. 5 shows two different simulations changing the radius of the perturbation region. The plot on the right shows a higher density of vortices than the plot on the left, but as Fig. 6 indicates, the density distribution is similar in both cases. In the first case, the stationary state is reached with a total number of around 400 vortices inside the domain, while in the case for $k_r = 128$ the total number of vortices is roughly 3300.

We conclude this section by analyzing certain properties of the point vortex model to compare them with the Navier-Stokes simulations. First, Fig. 6 represents the density profile of the number of vortices as a function of the distance to the center of the box. This density is a linear density, by means that it is defined as the number of vortices in a thin annulus inside the domain divided by the radius of the annulus. The curves for different sizes of the forcing region are shown in that plot. The reader may observe that all the curves follow a similar behavior. A note should be done at this point. Unlike the other curves, the curve corresponding to the region with $k_r = 256$ is slightly below the others. This discrepancy arises because the stationary state for that simulation had not yet been reached by the end of the run. Despite this, the curve remains consistent with the others. The reader may also observe a interesting power law $\propto 1/r$ which fits reasonably well in the middle region of the range of r. This in turn implies a constant flux of vortices in that subregion.

Fig. 7 shows a mean radius weighted with the number of vortices as a function of time, according to its definition in Eq. (2.39). This simulation differs from the others in the point vortex problem in that

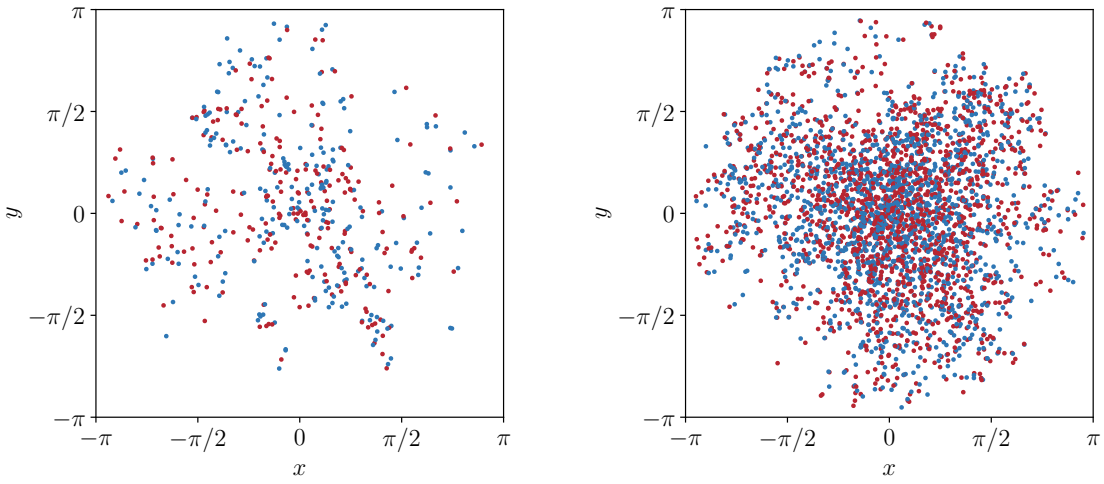

(a) $k_r = 16$ **(b)** $k_r = 128$

Figure 5: Evolution of the point vortex simulation for different sizes of the perturbation region. Red colors and blue colors mean different direction of rotation for each vortex.

no vortices are removed at any time, making the integration domain the entire $\mathbb{R}^2$. This is done to avoid the appearance of a stationary state in the system. As a first observation, the reader observes a growing behavior which resembles, in the middle stages, to the behavior of the enstrophy mean radius in the Navier-Stokes simulations (see Fig. 4b). It has been proved that the curve is well fitted with the law $A\sqrt{t}$, except for the very early times. As time increases and vortices evolve to the outer regions of the domain, the curve starts to differ from the ones observe in the Navier-Stokes simulations. This may be attributed to the effect of the boundary conditions. In the Navier-Stokes simulations, the boundary conditions are periodic, thus allowing the vortices to travel *backwards* towards the center of the domain. In the point vortex simulations, the domain is open and the tendency of pairs of vortices to travel in an almost straight line, due to its similar magnitude of circulation, is not blocked.

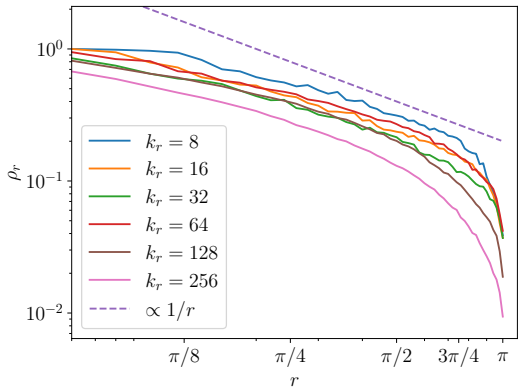

Figure 6: Density profile of the number of vortices as a function of the distance to the center of the perturbation region. The curves are averaged once a stationary state is reached and then they are normalized by their maximum value which is attained near the forcing region.

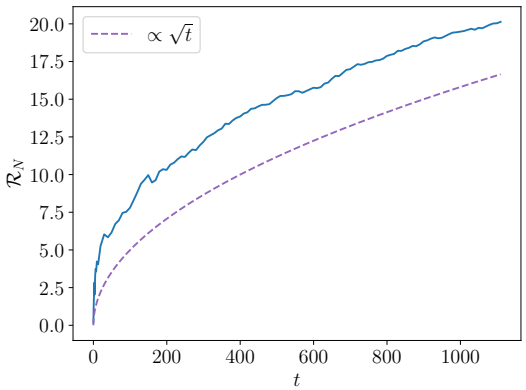

Figure 7: Mean radius weighted with the number of vortices (following the definition in Eq. (2.39)) as a function of time. The units of time are those determined from the circulation Γ of the vortices and the natural length-scale k_r^{-1}, giving $1/(\Gamma k_r^2)$.

4 Conclusions

This article has demonstrated that locally injected turbulence in a 2D space spreads to the boundaries of the domain, provided the Reynolds number is sufficiently high. This is in contrast to previous works in 3D domains, where the energy is shown to be confined to the region of the forcing. The results of the Navier-Stokes simulations show that the enstrophy density distribution is consistent with the point vortex simulations, where the vortices spreads across the domain and reaches the boundaries. This is observed for different values of the size of the forcing region k_r and the Reynolds number. Moreover, the profile of the energy and enstrophy density distributions as a function of the radius from the center of the domain has been claimed to follow a power law of A/r^2, for some constant A. Particularly in the case of enstrophy, the results show remarkable consistency, suggesting that as $k_r \to 0$ and sufficient time elapses, the power law for the enstrophy density distribution is expected to cover the entire range of r.

Regarding the point vortex simulations, the findings indicate that the power law A/r provides a good approximation for the density distribution of vortices per unit length ρ_r This contrasts with the results from Navier-Stokes simulations, where the enstrophy density distribution is better described by a power law A/r^2. This discrepancy implies, as illustrated in the figures above, a faster decay of enstrophy in Navier-Stokes simulations compared to the point-vortex model. This suggests the need to identify a more accurate metric for comparing both models.

For an extension of this work, it would be interesting to run the simulations for a longer time and higher values of k_r and Re for the embarrassingly parallel code. This would allow for a more accurate determination of the accordance of the plots for the evolution of the mean radii in both the Navier-Stokes and the point vortex simulations. Finally, these results could be replicated with the addition of a drag force $-\alpha \boldsymbol{u}$ to the Navier-Stokes equations, where α is a constant. This would allow us to investigate whether the energy still spreads as far as the domain allows, even in the presence of the drag force. To account that in the point vortex model, an extra equation is suggested to be added to the pair of equations for x_i and y_i. This equation would concentrate the drag effect on the intensity of circulation of the point vortex, formulated as

$$\dot{\Gamma}_i = -\beta \Gamma_i \tag{4.1}$$

for some constant β.

Acknowledgements

I would not like to finish this project without thanking the people who have helped me along the way. First and foremost, I would like to thank my two supervisors, Prof. Alexandros Alexakis and Prof. Emmanuel Dormy, for their guidance and constant support throughout the project. This project was, in the theoretical perspective, a bit far from my previous works, but their continuous help and advice made it possible. I would also like to thank the whole group led by Professor Stéphan Fauve in the Laboratoire de Physique de l'École Normale Supérieure, for giving me a desk and a place to work during my internship. Finally, I appreciate the huge amount of time and resources that both supercomputer centers, IDRIS and MESOPSL, have provided me during the development of this project. Without their technological resources, this project would have been impossible to carry out.

References

Alexakis, A. and L. Biferale (2018). "Cascades and transitions in turbulent flows." In: *Physics Reports* 767-769. Cascades and transitions in turbulent flows, pp. 1–101. ISSN: 0370-1573. DOI: 10.1016/j.physrep.2018.08.001.

Alexakis, A. (2023). "How far does turbulence spread?" In: *Journal of Fluid Mechanics* 977, R1. DOI: 10.1017/jfm.2023.951.

Aref, H. (2007). "Point vortex dynamics: A classical mathematics playground." In: *Journal of Mathematical Physics* 48.6, p. 065401. ISSN: 0022-2488. DOI: 10.1063/1.2425103.

Batchelor, G. K. (2000). *An Introduction to Fluid Dynamics*. Cambridge Mathematical Library. Cambridge University Press.

Boffetta, G. and R. E. Ecke (2012). "Two-Dimensional Turbulence." In: *Annual Review of Fluid Mechanics* 44.Volume 44, 2012, pp. 427–451. ISSN: 1545-4479. DOI: 10.1146/annurev-fluid-120710-101240.

Brachet, M. E. et al. (2008). *High-order low-storage explicit Runge-Kutta schemes for equations with quadratic nonlinearities*. arXiv: 0808.1883.

Ceci, S. and C. Seis (2022). "On the dynamics of point vortices for the two-dimensional Euler equation with L^p vorticity." In: *Philosophical Transactions of the Royal Society A: Mathematical, Physical and Engineering Sciences* 380.2226, p. 20210046. DOI: 10.1098/rsta.2021.0046.

Frisch, U. (1995). *Turbulence: The Legacy of A. N. Kolmogorov*. Cambridge University Press.

Griffiths, D. J. (2023). *Introduction to Electrodynamics*. 5th ed. Cambridge University Press.

Mininni, P. D. et al. (2011). "A hybrid MPI-OpenMP scheme for scalable parallel pseudospectral computations for fluid turbulence." In: *Parallel Computing* 37.6, pp. 316–326. ISSN: 0167-8191. DOI: 10.1016/j.parco.2011.05.004.

Saffman, P. G. (1993). *Vortex Dynamics*. Cambridge Monographs on Mechanics. Cambridge University Press.